

$d+id'$ Chiral Superconductivity in Bilayer Silicene

Feng Liu^{†,1,2} Cheng-Cheng Liu^{†,1,3} Kehui Wu,³ Fan Yang^{*,1} and Yugui Yao^{1,3,*}

¹School of Physics, Beijing Institute of Technology, Beijing 100081, China

²State Key Laboratory of Nonlinear Mechanics, Institute of Mechanics, Chinese Academy of Sciences, Beijing, 100190, China

³Beijing National Laboratory for Condensed Matter Physics and Institute of Physics, Chinese Academy of Sciences, Beijing 100190, China

We investigate the structure and physical properties of the undoped bilayer silicene (BLS). Our first principle (FP) calculations reveal that the band structure of the system with D_{3d} symmetry is intrinsically metallic with pocket Fermi surfaces around each K point, which opens the door to formation of a superconducting state. Our further study based on random phase approximation (RPA) identifies the system as a chiral $d+id'$ superconductor, mediated by the strong spin fluctuation on border of the antiferromagnetic spin density wave (SDW) order. Tunable Fermi pocket area via strain enables high superconducting critical temperature, which emerges when the SDW critical interaction strength is tuned near that of the real interaction. Our discovery not only sheds light upon the realization of the long-sought chiral $d+id'$ superconductivity (SC), but will also bring the exotic unconventional SC into the familiar Si-industry.

Chiral SC is a special kind of topological SC characterized by time reversal symmetry breaking¹. In the past few years, a surge of theoretical proposals have been raised on the experimental realization of this kind of unconventional SC, including such examples as the triplet $p_x \pm ip_y$ ($p+ip'$) pairing²⁻⁴ and the singlet $d_{x^2-y^2} \pm id_{xy}$ ($d+id'$) pairing⁵⁻¹³. While the former has probably been realized in the Sr_2RuO_4 system¹⁴, no experimental evidence has now been detected for the latter although the cuprates family⁵⁻⁷ and more probably the doped graphene⁸⁻¹³ have been proposed as possible candidates. Here, we predict the realization of the singlet $d+id'$ SC in the undoped BLS, which is easier than to dope the graphene system. As a result of its nontrivial topological property, this intriguing pairing state will bring a series of interesting experimental consequences such as quantized boundary current⁵, spontaneous magnetization^{5,7} and quantized spin and thermal Hall conductance⁷.

Silicene, considered as the silicon-based counterpart of the graphene, has attracted much attention both theoretically and experimentally¹⁵⁻²⁷. Similar honeycomb lattice structure of the two systems let them share most of their marvellous physical properties, including gapless Dirac fermions at the Brillouin-Zone corner, and the quantum spin Hall effect when spin-orbital coupling turns on^{16,17}. Remarkable difference between the graphene and the silicene systems mainly lies in the nonplanar low-buckled (LB) lattice structure of the latter^{16,18}, which originates from the weakened π -bond between neighboring silicon atoms. Just like the bilayer graphene (BLG), silicene can also take the form of its bilayer version, which has recently been synthesized²⁴. However, due to the LB structure of each silicene layer, there are actually different stacking ways between the silicene bilayer, including the one studied in the Ref²⁸, which might not be energetically optimized. Thus, it is necessary to identify the realized stacking ways and the stability of the bilayer structure of the system.

In this paper, we first identify the AB-bt bilayer structure (introduced below) as the energetically most favored one through FP calculations, and find that the corresponding electronic band structure is intrinsically metallic for the undoped case with much larger Fermi pockets than the BLG²⁹, opening the door to formation of a superconducting state. We further

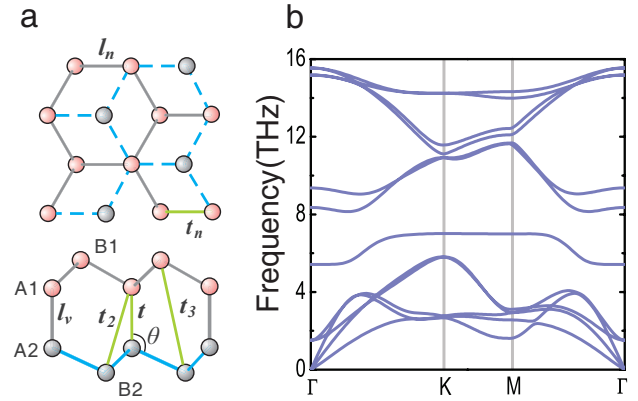


FIG. 1. **Geometry and phonon spectrum of the BLS.** **a**, Optimized geometry of the BLS. **b**, The corresponding phonon spectrum. In **a**, both the top view (upper) and side view (lower) are shown. The vertical bond length l_v , the nearest-neighbor in plane bond length l_n , and the angle θ between them are marked, together with the hopping integrals between each two of the four atoms A_i, B_i ($i = 1, 2$) within a unit cell.

did a RPA based study of the system when realistic Hubbard-interaction is added into our tight-binding (TB) model. Subsequently, a collinear antiferromagnetic SDW order is found at realizable interaction parameters. Interestingly, below but near the SDW critical point which is tunable via strain, a chiral $d+id'$ pairing state emerges with possibly high superconducting critical temperature, mediated by the strong spin fluctuation on border of the SDW order. The exotic chiral $d+id'$ SC in the BLS can thus be manipulated via strain, which opens prospects for both studying the unconventional topological SC in new playground and for applications in the Si based electronics.

Crystal and Band Structure: The crystal and electronic band structures of the BLS reported below are obtained through our FP calculations based on Density functional theory (DFT). The electronic band structure of the system is obtained self-consistently by using the projector augmented wave (PAW) pseudopotential method implemented in

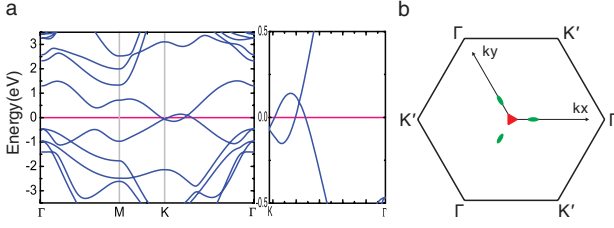


FIG. 2. **Band structure of the BLS.** **a**, The band structure of BLS corresponding to the optimized structure. **b**, The FS patches around each K point. In **a**, zooming in the low energy band (right) is also shown. In **b**, the central pocket (red) is electron-like and the outer three identical pockets (green) are hole-like, where the total areas of the two kinds of pockets are equal.

the VASP package³⁰. The exchange-correlation potential is treated by Perdew-Burke-Ernzerhof (PBE) potential³¹.

As a consequence of the LB structure of each silicene layer, there are actually four stacking ways (see Supplementary information I) between the upper and lower layers in the system. Our FP calculations revealed that two of them are stable, among which the energetically favored one (named as the AB-bt structure) is shown in Fig. 1a, and the corresponding phonon spectrum³² is shown in Fig. 1b.

From Fig. 1a, the bottom (A_1 -sublattice) of the upper silicene layer couples with the top (A_2 -sublattice) of the lower layer vertically with a bond-length $l_v = 2.53\text{\AA}$, while the two sublattices (A and B) within a layer couples with a bond-length $l_n = 2.32\text{\AA}$. Approximately equal bond lengths, together with the bond-angle $\theta = 106.60^\circ$ between the two bonds describes an orbital hybridization more like the sp^3 type (with bond angle $\theta = 109.47^\circ$) than the planar sp^2 type. From Fig. 1b, the phonon frequencies obtained are real at all momenta, which suggests a stable structure. The energy of this configuration is -19.65eV per unit cell, lower than that of the configuration studied in the literature²⁸, which is -19.51eV per unit cell. It's noting here that the symmetry group of the system is D_{3d} .

The band structure of the BLS with AB-bt stacking way is shown in Fig. 2a (left), together with its low energy zooming in (right). The most obvious feature of this band structure is the 300meV overlap between the valence band and the conduction band, much larger than the 1.6meV in the BLG and the 40meV in the graphite. Another important feature is the asymmetric band crossings present not only at the K point, but also on the K- Γ axis with an energy difference between them. Such an asymmetric band crossing results in a three-folded symmetric pocket Fermi surface (FS) structure surrounding each K point, as shown in Fig. 2b, where the central electron pocket is accompanied by three identical outer hole pockets with equal total area. Here, only the FS patches around one K point are present. The other patches can be obtained by six-folded rotations around the Γ point, as required by the D_{3d} symmetry and the time reversal invariant of the system.

To proceed, we construct the following effective 4-band TB

TABLE I. TB parameters fitted for the BLS in comparison with those of the BLG³³. The unit is eV.

	t_n	t	t_2	t_3	Δ
AB-bt	1.13	2.025	0.15	0.62	-0.0691
BLG	3.12	0.377	0.12	0.29	-0.0366

model in the basis $\{|B_1\rangle, |B_2\rangle, |A_1\rangle, |A_2\rangle\}$, which well captures all the low energy features of the above band structure near the FS,

$$H(\mathbf{k}) = \begin{pmatrix} \Delta & t_3 f(\mathbf{k}) & t_n f(\mathbf{k})^* & -t_2 f(\mathbf{k})^* \\ t_3 f(\mathbf{k})^* & \Delta & -t_2 f(\mathbf{k}) & t_n f(\mathbf{k}) \\ t_n f(\mathbf{k}) & -t_2 f(\mathbf{k})^* & 0 & t \\ -t_2 f(\mathbf{k}) & t_n f(\mathbf{k})^* & t & 0 \end{pmatrix}. \quad (1)$$

Here A_i, B_i ($i = 1, 2$) represent the basis mainly composed of the $3p_z$ -orbitals localized around each of the four silicon atoms within a unit cell. The hopping integrals t_n, t, t_2 and t_3 between each two orbitals are marked in Fig. 1a. The phase factor $f(\mathbf{k}) = \sum_{\alpha} e^{i\mathbf{k} \cdot \mathbf{R}_{\alpha}}$, with \mathbf{R}_{α} ($\alpha = 1, 2, 3$) to be the nearest-neighbor vector. Finally, notice the small effective on site energy difference Δ between the A and B atoms. The fitted parameters of the system in comparison with those of the BLG are listed in Table I, from which the most obvious feature of the BLS lies in the dominating role of the vertical inter-layer hopping t . The resulting strong bonding-antibonding energy split between A_1 and A_2 orbitals pushes them far away from the Fermi level, leaving B_1 and B_2 orbitals to form a low energy subspace which takes responsibility for the main physics of the system.

It's important to point out here that the low energy band structure of the system is considerably sensitive to the biaxial strain exerted on each silicene layer. As shown in Fig. 3c, for small strains which keep the symmetry and FS topology of the system, the total area of the electron or hole pockets feels a considerable variation. This tunable property of the band structure turns out to be very important for our following discussions.

RPA and SDW: Let's consider the following 4-band Hubbard-model of the system,

$$H = \sum_{\mathbf{k}\sigma, \alpha\beta} c_{\mathbf{k}\alpha\sigma}^{\dagger} H_{\alpha\beta}(\mathbf{k}) c_{\mathbf{k}\beta\sigma} + U \sum_{i, \alpha=1,4} n_{i\alpha\uparrow} n_{i\alpha\downarrow}, \quad (2)$$

where $H(\mathbf{k})$ is defined by (1), i and α (β) denote the unit cell and orbital indices respectively. Standard multi-orbital random phase approximation (RPA)³⁴⁻³⁹ (see also Supplementary information II) approach is adopted in our study.

The free susceptibility ($U = 0$) of the model is,

$$\chi_{l_3, l_4}^{(0)l_1, l_2}(\mathbf{q}, \tau) \equiv \sum_{\mathbf{k}_1, \mathbf{k}_2} \left\langle T_{\tau} c_{l_1}^{\dagger}(\mathbf{k}_1, \tau) c_{l_2}(\mathbf{k}_1 + \mathbf{q}, \tau) c_{l_3}^{\dagger}(\mathbf{k}_2 + \mathbf{q}, 0) c_{l_4}(\mathbf{k}_2, 0) \right\rangle_0, \quad (3)$$

where l_i ($i = 1, \dots, 4$) denotes orbital index. The \mathbf{k} de-

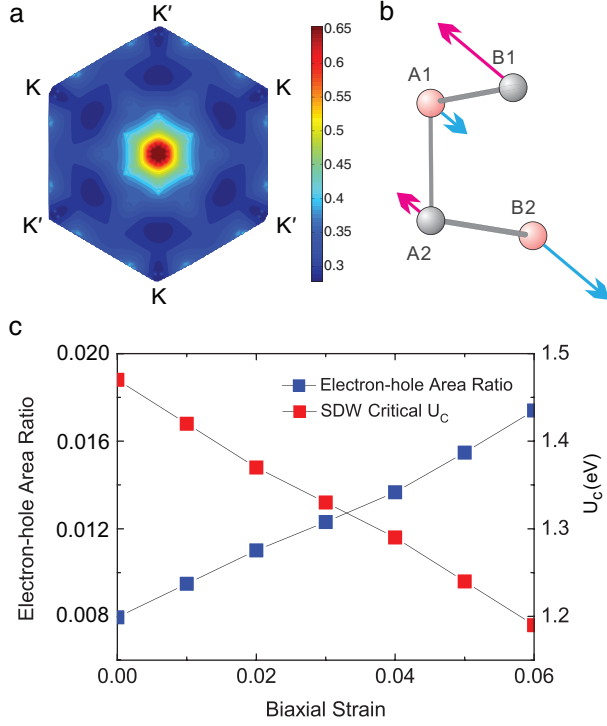


FIG. 3. **Free static susceptibility, the SDW ordered spin pattern and the biaxial strain-dependence of Fermi pocket area ratio and the SDW critical interaction strength.** **a**, k -dependence of the free static susceptibility. **b**, The SDW ordered spin pattern. **c**, The biaxial strain-dependence of Fermi pocket area ratio, viz, the ratio of the total area of the electron and hole pockets against the total area of Brillouin Zone, and the SDW critical value U_c of the BLS.

pendent static susceptibility of the system defined by the largest eigenvalue of the susceptibility matrix $\chi_{l,m}^{(0)}(\mathbf{q}) \equiv \chi_{m,m}^{(0),l}(\mathbf{q}, i\nu = 0)$ is shown in Fig.3a, which displays a distribution centering around the Γ -point.

When interaction turns on, the spin ($\chi^{(s)}$) or charge ($\chi^{(c)}$) susceptibility in the RPA level is given by

$$\chi^{(s(c))}(\mathbf{q}, i\nu) = \left[I \mp \chi^{(0)}(\mathbf{q}, i\nu)(U) \right]^{-1} \chi^{(0)}(\mathbf{q}, i\nu). \quad (4)$$

Here (U) is 16×16 matrix, whose only four nonzero elements are $(U)_{\mu\mu}^{\mu\mu} = U$ ($\mu = 1, \dots, 4$). It's clear that the repulsive Hubbard-interaction suppresses $\chi^{(c)}$ and enhances $\chi^{(s)}$. When the interaction strength U is enhanced to a critical value U_c , the spin susceptibility of the model diverges, which implies the instability toward long-range SDW order. The ordered spin structure of this bilayer system determined by the eigenvector of the spin susceptibility matrix $\chi_{l,m}^{(s)}(\mathbf{q}) \equiv \chi_{m,m}^{(s),l}(\mathbf{q}, i\nu = 0)$ corresponding to its largest eigenvalue is shown in Fig.3b, from which one finds an antiferromagnetic state with antiparallelly aligned spin patterns within a unit cell. The ordered moments are mainly distributed on the B_i ($i = 1, 2$) atoms which take responsibility for the low energy physics of the system. It's noting here that with the enhance-

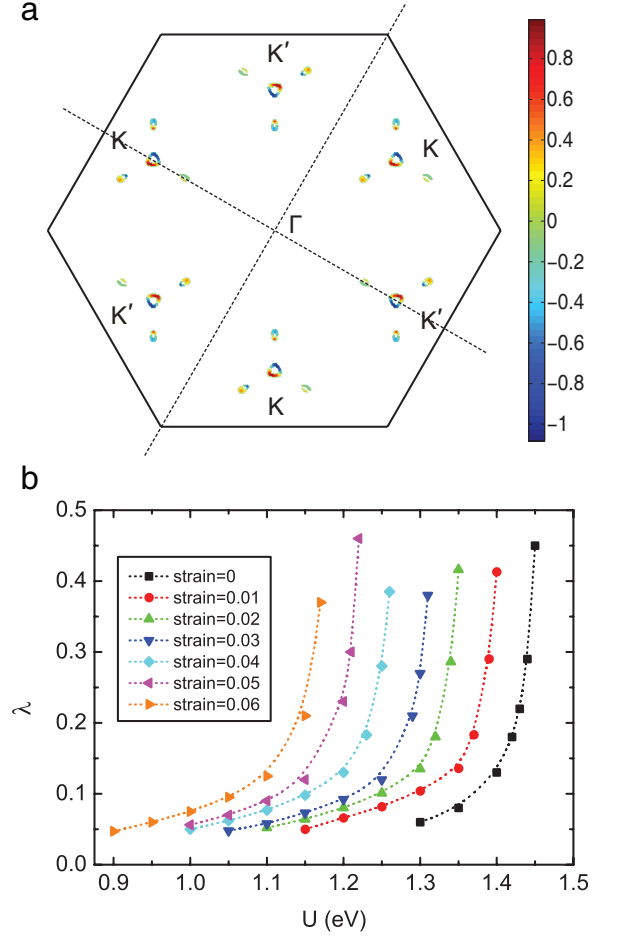


FIG. 4. **k -dependence of the gap function of the $d_{x^2-y^2}$ symmetry and the interaction strength U dependence of the largest eigenvalue λ of the linearized gap function.** **a**, k -dependence of the gap function of the $d_{x^2-y^2}$ symmetry, which is one of the leading symmetry of the system (the other one, i.e. the d_{xy} is shown in the Supplementary information III). **b**, The interaction strength U dependence of the largest eigenvalue λ of the linearized gap function (6), which is related to T_c through $T_c = 1.13\hbar\omega_D e^{-1/\lambda}$. In **a**, the gap function is antisymmetric about the axis $x = \pm y$ shown in the reciprocal space. In **b**, results for different strain values are shown.

ment of the strain and hence the Fermi pocket area, the SDW critical value U_c feels an obvious variation from the 1.48eV at zero strain to the 1.18eV at the strain of 0.06. Such a range is probably realizable for the Hubbard- U of the $3p_z$ orbitals of the silicon atoms.

Superconductivity: Through exchanging antiferromagnetic spin fluctuations between each cooper pair, unconventional chiral $d + id'$ SC emerges in the BLS system.

Let's consider the process when a cooper pair with momenta $(\mathbf{k}', -\mathbf{k}')$ in the β -th ($\beta = 1, 2$) band are scattered to $(\mathbf{k}, -\mathbf{k})$ in the α -th ($\alpha = 1, 2$) band by charge or spin fluctuations. This process results in the following effective interaction,

$$V_{eff} = \sum_{\alpha\beta, \mathbf{k}\mathbf{k}'} V^{\alpha\beta}(\mathbf{k}, \mathbf{k}') c_{\alpha}^{\dagger}(\mathbf{k}) c_{\alpha}^{\dagger}(-\mathbf{k}) c_{\beta}(-\mathbf{k}') c_{\beta}(\mathbf{k}'), \quad (5)$$

where the effective interaction vertex $V^{\alpha\beta}(\mathbf{k}, \mathbf{k}')$ determined by the RPA susceptibility (4) can be found in Ref³⁹ (see also Supplementary information II).

From this effective interaction, we obtained the following linearized gap equation³⁹ near T_c ,

$$-\frac{1}{(2\pi)^2} \sum_{\beta} \oint_{FS} dk'_{\parallel} \frac{V^{\alpha\beta}(\mathbf{k}, \mathbf{k}')}{v_F^{\beta}(\mathbf{k}')} \Delta_{\beta}(\mathbf{k}') = \lambda \Delta_{\alpha}(\mathbf{k}). \quad (6)$$

Here, the integration is along various FS patches labelled by α or β . The $v_F^{\beta}(\mathbf{k}')$ is Fermi velocity at \mathbf{k}' on the β -th FS patch, and k'_{\parallel} represents the component along that patch. In this eigenvalue problem, the normalized eigenvector $\Delta_{\alpha}(\mathbf{k})$ represents the relative value of the gap function on the α -th FS patches near T_c which is related to the eigenvalue λ through $T_c = 1.13\hbar\omega_D e^{-1/\lambda}$. Here $\hbar\omega_D$ is a typical energy scale for the spin or charge fluctuation, approximated as the low energy band width, i.e. $\hbar\omega_D \approx 300\text{meV}$. The leading pairing symmetry of the system is thus determined by the eigenvector $\Delta_{\alpha}(\mathbf{k})$ corresponding to the largest eigenvalue.

Our RPA calculations on the BLS identify an exactly degenerate d_{xy} and $d_{x^2-y^2}$ doublets as the leading pairing symmetry of the system for $U < U_c$ at all strain values, which is robust against small doping (see Supplementary information III). Both symmetries are singlet with nodal gap functions. While the $d_{x^2-y^2}$ shown in Fig.4a is antisymmetric about the axis $x = \pm y$ in the reciprocal space, the d_{xy} shown in Supplementary information III is symmetric about them. The two gap functions form a 2D E_g representation of the D_{3d} point-group of the system. For both symmetries, two gap nodes are present on each Fermi pocket. The U dependence of the eigenvalue λ which is related to T_c is shown in Fig.4b for different strains. Clearly, T_c increases with the Hubbard- U and rises promptly at $U/U_c \lesssim 1$ as a result of the strongly enhanced antiferromagnetic spin fluctuation near the critical point. Since U_c is tunable via strain as shown in Fig.3c, the ratio U/U_c varies within a range which provides basis for the realization of the relation $U/U_c \lesssim 1$ which is crucial for the high T_c of the system. For example, for $\lambda \approx 0.3$ attainable by different strains shown in Fig.4b, the T_c obtained can be as high as over 80K, although it is usually overestimated in the RPA level. For real material, whether high T_c can be acquired is determined by how near U/U_c can be tuned to 1.

Since the two d-wave pairing symmetries are degenerate, one would conjecture that they would probably be superposed⁴¹ to lower the energy below T_c . To determine how they are superposed at the ground state, let's set the gap function as $\Delta(\mathbf{k}) = \Delta_1 \Delta_{d_{x^2-y^2}}(\mathbf{k}) + \Delta_2 \Delta_{d_{xy}}(\mathbf{k})$, where the superposition coefficients Δ_i ($i = 1, 2$) are determined by minimization of the mean-field ground state energy of the effective Hamiltonian $H_{eff} = H_{band} + V_{eff}$. Here H_{band} is the kinetic part of (2) and V_{eff} is given by (5). Our energy minimization gives $\Delta_2 = i\Delta_1$, which just leads to the long sought nodeless chiral $d + id'$ SC! This superposition manner between the two d-wave pairings satisfies the requirement that the gap nodes should avoid the FS to lower the energy. With intrinsically complex gap functions, this pairing breaks time

reversal symmetry and will bring a lot of exotic properties. It is just a singlet analogy of the extensively studied $p + ip'$ SC.

Our RPA calculations for the system also identify a possible nodeless f-wave pairing to be the leading symmetry in the triplet channel. This pairing also breaks time reversal symmetry and the gap functions change sign with every 60° rotation, which belongs to A_{1u} representation of D_{3d} (see Supplementary information III). However, its T_c is much lower than that of the $d + id'$ pairing.

Conclusion: We have performed a FP calculation on the BLS. Through energy optimization, we identified an D_{3d} symmetric AB-bt stacking structure for the BLS. The band structure corresponding to this crystal structure is intrinsically metallic, with Fermi pockets around each K point whose areas are tunable via strain. We have further carried out a systematic RPA based study for the system. Our study suggests that above realizable interaction strength, collinear antiferromagnetic order will develop in the system. Below the SDW critical point U_c , a chiral $d + id'$ SC emerges in the system, whose T_c rises to its maximum at $U \lesssim U_c$ as a result of the strongly enhanced antiferromagnetic spin fluctuations near the critical point. Tunable U_c with strain makes high temperature SC possible in this system, the realization of which will bring a new epoch to the familiar Si-industry.

Acknowledgement. We are grateful to Dung-Hai Lee, Jun-Ren Shi, Fa Wang and Hong Yao for stimulating discussions. The work is supported by MOST Project of China (Grant No. 2011CBA00100) and NSF of China (Grants No. 10704008, 11274041, 10974231 and 11174337).

Author contributions. Y.G.Y. and F.Y. conceived the idea of searching for Chiral SC in the BLS, supervised the overall project and wrote the manuscript. Y.G.Y., F.L. and C.C.L. carried out the FP calculations and construct the effective TB model. F.Y. performed the RPA calculations. All the authors significantly contributed in the discussion and data analysis.

TABLE A.1. **Optimized energies and geometric parameters corresponding to the four possible structures of the BLS.** The second column gives the energy per unit cell. In the third column, the first and second number provide the bond-lengths of the nearest neighbor intra-layer and inter-layer valence bonds respectively. The final column is the angle between these two kinds of valence bonds. Note that in the AB-bb structure, the exchange symmetry between the upper and lower layers has been broken, as reflected in the different bond-lengths and bond-angles for the two layers.

Structure	Energy(eV)	Bond-length(Å)	Bond-Angle
AA-bb	-19.14	2.28, 5.12	101.52°
AA-bt	-19.51	2.32, 2.46	106.48°
AB-bt	-19.65	2.32, 2.53	106.60°
AB-bb	-19.30	2.31(2.34), 2.92	107.77°(109.53°)

A. POSSIBLE STRUCTURES

Due to the weakened π -bond between adjacent Si-atoms, the silicene layer possesses a low-buckled non-planar structure, which is different from that of the graphene. In this structure, a silicene layer is divided into two halves, i.e. the top and bottom, with each occupying one of the two sublattices (A and B) of the original honeycomb lattice. As a result of this non-planar structure of a silicene layer, there can be four possible stacking ways between the two layers in the bilayer silicene (BLS), i.e. the AA bottom-bottom (AA-bb), the AA bottom-top (AA-bt), the AB bottom-top (AB-bt), and the AB bottom-bottom (AB-bb). The geometries and phonon spectra corresponding to these four structures are shown in Fig.A.1, and the corresponding optimized energies and parameters are listed in Table A.1

From Fig.A.1, it's clear that the four possible structures of the system possess different symmetries. The AA-bb and AB-bt structures shown in Fig.A.1a and Fig.A.1c possess the D_{3d} symmetry, while the point group of the AA-bt structure shown in Fig.A.1b is D_{3h} . The AB-bb structure shown in Fig.A.1d has the smallest symmetry group among the four, i.e. C_{3v} , since the different bond-lengths and bond-angles between the two layers shown in Fig.A.1e and Table A.1. From the phonon spectra corresponding to these structures, one finds that Fig.A.1b and Fig.A.1d are unstable toward structure reconfiguration because of the imaginary frequencies obtained, leaving only the two symmetric structures shown in Fig.A.1a and Fig.A.1c as possible candidates of realized structure.

The AA-bb structure shown in Fig.A.1a can be considered as a simple analogy to the AA-stacked BLG which consists of two graphene layers weakly coupled through the van der Waals interaction. Consequently, one finds from Table A.1 that the inter-layer bond-length corresponding to this structure is extremely large. This structure is energetically worst although it is locally stable. The AA-bt structure shown in Fig.A.1b is just the one studied in Ref²⁸. Although the energy

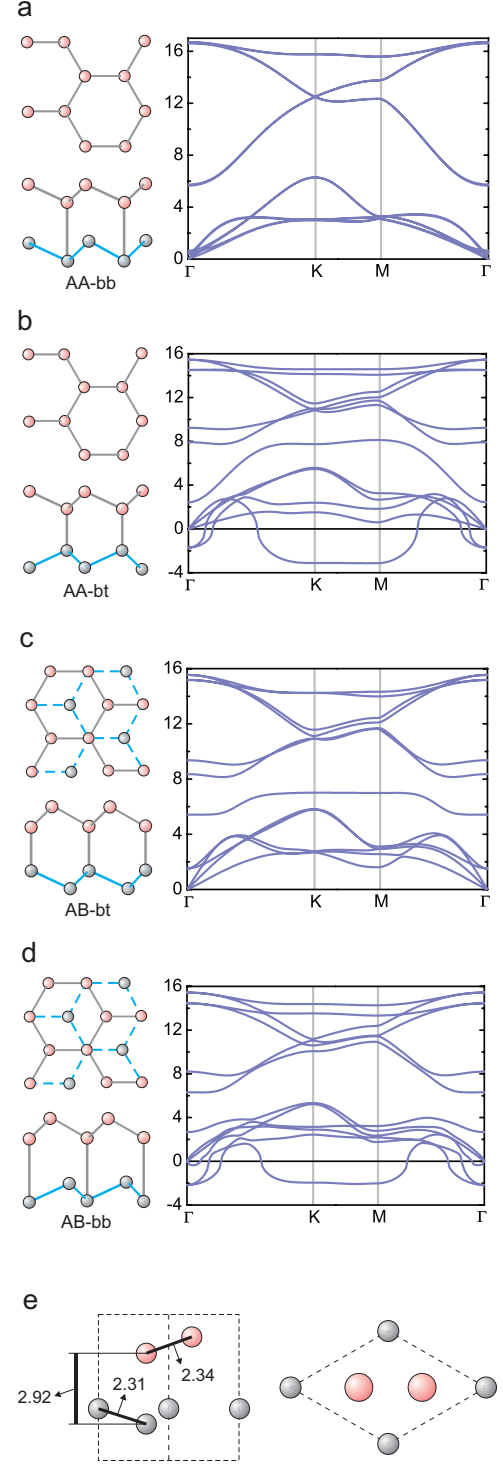


FIG. A.1. **Geometries and phonon spectra corresponding to the four possible structures of the BLS.** a-d, Geometries and phonon spectra for the AA-bb (a), AA-bt (b), AB-bt (c) and AB-bb (d) structures of the BLS. In each show, the left up is the top view, the left down is the side view and the right is the phonon spectrum corresponding to each structure. Note that negative frequencies shown actually represent imaginary values obtained and thus imply structure instability. e, More details for the configuration of the AB-bb structure, where one finds the breaking of the exchange symmetry between the two layers in this structure.

TABLE A.2. **TB parameters fitted for the BLS via different strain.** The unit is eV.

Strain	t_n	t	t_2	t_3	Δ
0.00	1.130	2.025	0.152	0.616	-0.069
0.01	1.079	1.974	0.159	0.595	-0.073
0.02	1.045	1.947	0.162	0.585	-0.077
0.03	1.012	1.924	0.163	0.573	-0.082
0.04	0.980	1.904	0.162	0.562	-0.088
0.05	0.948	1.878	0.161	0.551	-0.092
0.06	0.912	1.844	0.158	0.541	-0.100

of this structure is somewhat favorable, it is locally unstable. The structure Fig.A.1d is not energetically favored either. The realized structure of the BLS should be the AB-bt structure shown in Fig.A.1c which is focused in the present work as it is not only energetically most favored but also locally stable. The bond-angle of this structure is 106.60° , very near to that of the sp^3 hybridization, i.e 109.47° . The inter-layer bond-length is 2.53\AA , near to the 2.32\AA of the intra-layer bond-length. Combination of the two features describes an sp^3 -like orbital hybridization rather than a planar sp^2 -like one.

The band structures corresponding to the above four crystal structures are shown in Fig.A.2. In the AA-bb band structure shown in Fig.A.2a, two crossings slightly deviating from each K point are present at the Fermi level, which leads to a semi-metal ground state. This state is not favored by energy, as illustrated above. The AA-bt band structure shown in Fig.A.2b has been studied in Ref²⁸. The two crossings locating on the Γ -M and Γ -K lines are present at the Fermi level,

also leading to a semi-metal state. However, our FP calculations revealed that this state is neither energetically most favored nor stable. The AB-bt band structure shown in Fig.A.2c is the finally realized one. Large band overlap and asymmetric band crossings are present in this band structure, which leads to the pocket Fermi surface (FS) structure shown in Fig.A.2e. The six-folded rotation symmetry of the FS is required by the D_{3d} and time reversal symmetry of the system. From this realized band structure, one obtains an intrinsically metallic ground state with finite DOS at the Fermi level, which opens the door to formation of SC. The AB-bb band structure shown in Fig.A.2d is somewhat similar with Fig.A.2c in that it also possesses band overlap. However, it is energetically unfavored.

It's important that the biaxial strain exerted on each silicene layer has obvious influence on the low energy band structure of the system. In the following Table A.2, we list the tight-binding (TB) parameters fitted for each strain up to 0.06, under which the symmetry and FS topology of the system is kept.

B. FOUR-ORBITAL RPA

In this part, we provide details of the four-orbital random phase approximation (RPA) approach³⁴⁻³⁹ adopted in the study of the above Hubbard-model (formula (2) in the main text).

A. RPA susceptibility

Let's define,

$$\chi_{l_3, l_4}^{(0)l_1, l_2}(\mathbf{q}, \tau) \equiv \sum_{\mathbf{k}_1, \mathbf{k}_2} \left\langle T_\tau c_{l_1}^\dagger(\mathbf{k}_1, \tau) c_{l_2}(\mathbf{k}_1 + \mathbf{q}, \tau) c_{l_3}^\dagger(\mathbf{k}_2 + \mathbf{q}, 0) c_{l_4}(\mathbf{k}_2, 0) \right\rangle_0 \quad (\text{B.1})$$

to be the free susceptibility for $U = 0$, with l_i ($i = 1, \dots, 4$) denoting orbital index. The explicit formulism of $\chi^{(0)}$ in the momentum-frequency space is,

$$\chi_{l_3, l_4}^{(0)l_1, l_2}(\mathbf{q}, i\omega_n) = \frac{1}{N} \sum_{\mathbf{k}, \alpha, \beta} \xi_{l_4}^\alpha(\mathbf{k}) \xi_{l_1}^{\alpha,*}(\mathbf{k}) \xi_{l_2}^\beta(\mathbf{k} + \mathbf{q}) \xi_{l_3}^{\beta,*}(\mathbf{k} + \mathbf{q}) \frac{n_F(\varepsilon_{\mathbf{k}+\mathbf{q}}^\beta) - n_F(\varepsilon_{\mathbf{k}}^\alpha)}{i\omega_n + \varepsilon_{\mathbf{k}}^\alpha - \varepsilon_{\mathbf{k}+\mathbf{q}}^\beta}, \quad (\text{B.2})$$

where $\alpha, \beta = 1, \dots, 4$ are band indices, $\varepsilon_{\mathbf{k}}^\alpha$ and $\xi_{l_i}^\alpha(\mathbf{k})$ are the α -th eigenvalue and eigenvector of the $H(\mathbf{k})$ matrix (equation (1) in the main text) respectively and n_F is the Fermi-

Dirac distribution function.

When interaction turns on, we define the spin ($\chi^{(s)}$) and charge ($\chi^{(c)}$) susceptibility as follow,

$$\begin{aligned}
\chi_{l_3, l_4}^{(c)l_1, l_2}(\mathbf{q}, \tau) &\equiv \frac{1}{2} \sum_{\mathbf{k}_1, \mathbf{k}_2, \sigma_1, \sigma_2} \left\langle T_\tau C_{l_1, \sigma_1}^\dagger(\mathbf{k}_1, \tau) C_{l_2, \sigma_1}(\mathbf{k}_1 + \mathbf{q}, \tau) C_{l_3, \sigma_2}^+(\mathbf{k}_2 + \mathbf{q}, 0) C_{l_4, \sigma_2}(\mathbf{k}_2, 0) \right\rangle, \\
\chi_{l_3, l_4}^{(s^z)l_1, l_2}(\mathbf{q}, \tau) &\equiv \frac{1}{2} \sum_{\mathbf{k}_1, \mathbf{k}_2, \sigma_1, \sigma_2} \sigma_1 \sigma_2 \left\langle T_\tau C_{l_1, \sigma_1}^\dagger(\mathbf{k}_1, \tau) C_{l_2, \sigma_1}(\mathbf{k}_1 + \mathbf{q}, \tau) C_{l_3, \sigma_2}^+(\mathbf{k}_2 + \mathbf{q}, 0) C_{l_4, \sigma_2}(\mathbf{k}_2, 0) \right\rangle, \\
\chi_{l_3, l_4}^{(s^{+-})l_1, l_2}(\mathbf{q}, \tau) &\equiv \sum_{\mathbf{k}_1, \mathbf{k}_2} \left\langle T_\tau C_{l_1, \uparrow}^\dagger(\mathbf{k}_1, \tau) C_{l_2, \downarrow}(\mathbf{k}_1 + \mathbf{q}, \tau) C_{l_3, \downarrow}^+(\mathbf{k}_2 + \mathbf{q}, 0) C_{l_4, \uparrow}(\mathbf{k}_2, 0) \right\rangle, \\
\chi_{l_3, l_4}^{(s^{-+})l_1, l_2}(\mathbf{q}, \tau) &\equiv \sum_{\mathbf{k}_1, \mathbf{k}_2} \left\langle T_\tau C_{l_1, \downarrow}^\dagger(\mathbf{k}_1, \tau) C_{l_2, \uparrow}(\mathbf{k}_1 + \mathbf{q}, \tau) C_{l_3, \uparrow}^+(\mathbf{k}_2 + \mathbf{q}, 0) C_{l_4, \downarrow}(\mathbf{k}_2, 0) \right\rangle.
\end{aligned} \tag{B.3}$$

Note that in non-magnetic state we have $\chi^{(s^z)} = \chi^{(s^{+-})} = \chi^{(s^{-+})} \equiv \chi^{(s)}$, and when $U = 0$ we have $\chi^{(c)} = \chi^{(s)} = \chi^{(0)}$.

In the RPA level, the spin/charge susceptibility for the Hubbard-model (formula (2) in the main text) is,

$$\begin{aligned}
\chi^{(s)}(\mathbf{q}, i\nu) &= \left[I - \chi^{(0)}(\mathbf{q}, i\nu)(U) \right]^{-1} \chi^{(0)}(\mathbf{q}, i\nu), \\
\chi^{(c)}(\mathbf{q}, i\nu) &= \left[I + \chi^{(0)}(\mathbf{q}, i\nu)(U) \right]^{-1} \chi^{(0)}(\mathbf{q}, i\nu) \tag{B.4}
\end{aligned}$$

where $\chi^{(s(c))}(\mathbf{q}, i\nu_n)$, $\chi^{(0)}(\mathbf{q}, i\nu_n)$ and (U) are 16×16 matrices with elements of the matrix (U) to be $(U)_{\theta\xi}^{\mu\nu} = U\delta_{\mu=\nu=\theta=\xi}$.

B. Pairing symmetry

Let's consider a cooper pair with momentum/orbital $(\mathbf{k}'t, -\mathbf{k}'s)$, which could be scattered to $(\mathbf{k}p, -\mathbf{k}q)$ by charge or spin fluctuations. In the RPA level, The effective interaction induced by this process is as follow,

$$V_{eff}^{RPA} = \sum_{pqst, \mathbf{k}\mathbf{k}'} \Gamma_{st}^{pq}(k, k') c_p^\dagger(\mathbf{k}) c_q^\dagger(-\mathbf{k}) c_s(-\mathbf{k}') c_t(\mathbf{k}'), \tag{B.5}$$

In the singlet channel, the effective vertex $\Gamma_{st}^{pq}(k, k')$ is given as follow,

$$\begin{aligned}
\Gamma_{st}^{pq}(k, k') &= (U)_{qs}^{pt} + \frac{1}{4} \left\{ (U) \left[3\chi^{(s)}(k - k') - \chi^{(c)}(k - k') \right] (U) \right\}_{qs}^{pt} + \\
&\quad \frac{1}{4} \left\{ (U) \left[3\chi^{(s)}(k + k') - \chi^{(c)}(k + k') \right] (U) \right\}_{qt}^{ps},
\end{aligned} \tag{B.6}$$

while in the triplet channel, it is

$$\begin{aligned}
\Gamma_{st}^{pq}(k, k') &= -\frac{1}{4} \left\{ (U) \left[\chi^{(s)}(k - k') + \chi^{(c)}(k - k') \right] (U) \right\}_{qs}^{pt} + \\
&\quad \frac{1}{4} \left\{ (U) \left[\chi^{(s)}(k + k') + \chi^{(c)}(k + k') \right] (U) \right\}_{qt}^{ps}.
\end{aligned} \tag{B.7}$$

Notice that the vertex $\Gamma_{st}^{pq}(k, k')$ has been symmetrized for the singlet case and anti-symmetrized for the triplet case. Generally we neglect the frequency-dependence of Γ and replace it by $\Gamma_{st}^{pq}(k, k') \approx \Gamma_{st}^{pq}(\mathbf{k}, \mathbf{k}', 0)$.

Projecting the above effective interaction (B.5) into the two bands which cross the FS, we obtain the following low energy effective Hamiltonian for the cooper pairs near the FS,

$$V_{eff} = \sum_{\alpha\beta, \mathbf{k}\mathbf{k}'} V^{\alpha\beta}(\mathbf{k}, \mathbf{k}') c_\alpha^\dagger(\mathbf{k}) c_\alpha^\dagger(-\mathbf{k}) c_\beta(-\mathbf{k}') c_\beta(\mathbf{k}'), \tag{B.8}$$

where $\alpha, \beta = 1, 2$ and $V^{\alpha\beta}(\mathbf{k}, \mathbf{k}')$ is

$$V^{\alpha\beta}(\mathbf{k}, \mathbf{k}') = \text{Re} \sum_{pqst, \mathbf{k}\mathbf{k}'} \Gamma_{st}^{pq}(\mathbf{k}, \mathbf{k}', 0) \xi_p^{\alpha,*}(\mathbf{k}) \xi_q^{\alpha,*}(-\mathbf{k}) \xi_s^\beta(-\mathbf{k}') \xi_t^\beta(\mathbf{k}'). \tag{B.9}$$

Here only intra-band pairing is considered for small U .

From the low energy effective Hamiltonian (B.8), one can obtain the following linearized gap equation³⁹ to determine the T_c and the leading pairing symmetry of the system,

$$-\frac{1}{(2\pi)^2} \sum_{\beta} \oint_{FS} dk'_{\parallel} \frac{V^{\alpha\beta}(\mathbf{k}, \mathbf{k}')}{v_F^{\beta}(\mathbf{k}')} \Delta_{\beta}(\mathbf{k}') = \lambda \Delta_{\alpha}(\mathbf{k}). \quad (\text{B.10})$$

Here, the integration and summation is along various FS patches labelled by α or β . The $v_F^{\beta}(\mathbf{k}')$ is Fermi velocity at \mathbf{k}' on the β -th FS patch, and k'_{\parallel} represents the component along that patch. In this eigenvalue problem, the normalized eigenvector $\Delta_{\alpha}(\mathbf{k})$ represents the relative value of the gap function on the α -th FS patches near T_c determined by

$$T_c = 1.13\hbar\omega_D e^{-1/\lambda}. \quad (\text{B.11})$$

The leading pairing symmetry of the system is thus determined by the largest eigenvalue λ of Eq.(B.10).

C. MORE DETAILS OF THE PAIRING SYMMETRIES OBTAINED

Our RPA calculations reveal that at half-filling, the leading pairing symmetries in the BLS are the $d_{x^2-y^2}$ and d_{xy} dou-

plets. The two gap functions are symmetry related: one is obtained from the other through the symmetry operations of D_{3d} , and thus they are exactly degenerate. While the normalized relative gap function of the $d_{x^2-y^2}$ symmetry has been shown in Fig.4a of the main text, here we provide that of the d_{xy} symmetry in Fig.C.1a. Obviously, the gap function for this pairing is symmetric about the axis $x = \pm y$ shown in the reciprocal space.

It is interesting that our RPA calculations also identify a possible f-wave SC shown in Fig.C.1b to be the leading one in the triplet channel at half-filling. The gap function of this pairing changes sign with every 60° rotation. It is antisymmetric about the three diagonal lines shown in the Brillouin-Zone, which are just the gap node lines. This gap function belongs to A_{1u} irreducible representation of D_{3d} . Similarly with the $d + id'$ symmetry, this pairing also satisfies the requirement that gap nodes should avoid the FS. Positive eigenvalue λ corresponding to this symmetry suggests finite T_c of the pairing, which is nevertheless much lower than that of the $d + id'$ symmetry.

The $d + id'$ pairing found here is robust against small doping. Our RPA calculations yield that for $U = 1\text{eV}$, the leading pairing symmetry of the system is still $d + id'$ either for the 5% electron-doped case shown in Fig.C.2a or for the 5% hole-doped case shown in Fig.C.2b although the FS topology has been modified.

* email:ygyao@bit.edu.cn.

*email:yangfan_blg@bit.edu.cn.

[†]These authors contributed equally to this work.

- ¹ Sigrist, M. & Ueda, K. Phenomenological theory of unconventional superconductivity. *Rev. Mod. Phys.* **63**, 239–311 (1991).
- ² Fu, L. & Kane, C.L. Superconducting Proximity Effect and Majorana Fermions at the Surface of a Topological Insulator. *Phys. Rev. Lett.* **100**, 096407 (2008).
- ³ Qi, X.L., Hughes, T., Raghu, S., & Zhang, S.C. Time-Reversal-Invariant Topological Superconductors and Superfluids in Two and Three Dimensions. *Phys. Rev. Lett.* **102**, 187001 (2009).
- ⁴ Cheng, M., Sun, K., Galitski, V. & Das Sarma, S. Stable topological superconductivity in a family of two-dimensional fermion models. *Phys. Rev. B* **81**, 024504 (2010).
- ⁵ Laughlin, R.B. Magnetic Induction of $d_{x^2-y^2} + id_{xy}$ Order in High- T_c Superconductors. *Phys. Rev. Lett.* **80**, 5188–5191 (1998).
- ⁶ Vojta, M., Zhang, Y. & Sachdev, S. Quantum phase transitions in d-wave superconductors. *Phys. Rev. Lett.* **85**, 4940–4943 (2000).
- ⁷ Horovitz, B. & Golub, A. Superconductors with broken time-reversal symmetry: Spontaneous magnetization and quantum Hall effects. *Phys. Rev. B* **68**, 214503 (2003).
- ⁸ Black-Schaffer, A.M. & Doniach, S. Resonating valence bonds and mean-field d-wave superconductivity in graphite. *Phys. Rev. B* **75**, 134512 (2007).
- ⁹ Gonzalez, J. Kohn Luttinger superconductivity in Graphene. *Phys. Rev. B* **78**, 205431 (2008).
- ¹⁰ Pathak, S., Shenoy, V.B. & Baskaran, G. Possibility of High T_c Superconductivity in doped Graphene. *Phys. Rev. B* **81**, 085431 (2010).
- ¹¹ Nandkishore, R., Levitov, L.S. & Chubukov A.V. Chiral superconductivity from repulsive interactions in doped graphene. *Nature Phys.* **8**, 158–163 (2012).
- ¹² Kiesel, M. L. *et al.* Competing many-body instabilities and unconventional superconductivity in graphene. *Phys. Rev. B* **86**, 020507(R) (2012).
- ¹³ Wang, W.S. *et al.* Functional renormalization group and variational Monte Carlo studies of the electronic instabilities in graphene near 1/4 doping. *Phys. Rev. B* **85**, 035414 (2012).
- ¹⁴ Mackenzie, A.P. & Maeno, Y. The superconductivity of Sr_2RuO_4 and the physics of spin-triplet pairing. *Rev. Mod. Phys.* **75**, 657–712 (2003).
- ¹⁵ Guzmán-Verri, G. G. & Lew Yan Voon, L. C. Electronic structure of silicon-based nanostructures. *Phys. Rev. B* **76**, 075131 (2007).
- ¹⁶ Liu, C.-C., Feng, W. & Yao, Y. Quantum Spin Hall Effect in Silicene and Two-Dimensional Germanium. *Phys. Rev. Lett.* **107**, 076802 (2011).
- ¹⁷ Liu, C.-C., Jiang, H. & Yao, Y. Low-energy effective Hamiltonian involving spin-orbit coupling in silicene and two-dimensional germanium and tin. *Phys. Rev. B* **84**, 10195430 (2011).
- ¹⁸ Cahangirov, S., Topsakal, M., Aktürk, E., Şahin, H. & Ciraci, S. Two- and One-Dimensional Honeycomb Structures of Silicon and Germanium. *Phys. Rev. Lett.* **102**, 236804 (2009).
- ¹⁹ Ezawa, M. Valley-Polarized Metals and Quantum Anomalous Hall Effect in Silicene. *Phys. Rev. Lett.* **109**, 055502 (2012).
- ²⁰ Ezawa, M. A topological insulator and helical zero mode in silicene under an inhomogeneous electric field. *New J. Phys.* **14**, 033003 (2012).
- ²¹ Ezawa, M. Quasi-Topological Insulator and Trigonal Warping in Gated Bilayer Silicene. arXiv:1204.3971 (2012).
- ²² Lalmi, B. *et al.* Epitaxial growth of a silicene sheet. *Appl. Phys.*

- Lett.* **97**, 223109 (2010).
- ²³ Chen, L. *et al.* Evidence for Dirac Fermions in a honeycomb lattice based on silicon. *Phys. Rev. Lett.* **109**, 056804 (2012).
 - ²⁴ Feng, B. *et al.* Evidence of Silicene in Honeycomb Structures of Silicon on Ag(111). *Nano Lett.* **12**, 3507 (2012).
 - ²⁵ Vogt, P. *et al.* Silicene: Compelling Experimental Evidence for Graphenelike Two-Dimensional Silicon. *Phys. Rev. Lett.* **108**, 155501 (2012).
 - ²⁶ Fleurence, A. *et al.* Experimental Evidence for Epitaxial Silicene on Diboride Thin Films. *Phys. Rev. Lett.* **108**, 245501 (2012).
 - ²⁷ Kara, A. *et al.* A review on silicene — New candidate for electronics. *Surf. Sci. Rep.* **67**, 1–18 (2012).
 - ²⁸ Morishita, T. *et al.* First-principles study of structural and electronic properties of ultrathin silicon nanosheets. *Phys. Rev. B* **82**, 045419 (2010).
 - ²⁹ McCann, E. & Falco, V. I. Landau-Level Degeneracy and Quantum Hall Effect in a Graphite Bilayer. *Phys. Rev. Lett.* **96**, 086805 (2006).
 - ³⁰ Kresse, G. & Furthmüller, J. Efficient iterative schemes for ab initio total-energy calculations using a plane-wave basis set. *Phys. Rev. B* **54**, 11169 (1996).
 - ³¹ Perdew, J. P., Burke, K. & Ernzerhof, M. Generalized Gradient Approximation Made Simple. *Phys. Rev. Lett.* **77**, 3865 (1996).
 - ³² Togo, A., Oba, F. & Tanaka, I. First-principles calculations of the ferroelastic transition between rutile-type and CaCl_2 -type SiO_2 at high pressures. *Phys. Rev. B* **78**, 134106 (2008).
 - ³³ Partoens, B. & Peeters, F. M. From graphene to graphite: Electronic structure around the K point. *Phys. Rev. B* **74**, 075404 (2006).
 - ³⁴ Takimoto, T., Hotta, T. & Ueda, K. Strong-coupling theory of superconductivity in a degenerate Hubbard model. *Phys. Rev. B* **69**, 104504 (2004).
 - ³⁵ Yada, K. & Kontani, H. Origin of the Weak Pseudo-gap Behaviors in $\text{Na}_{0.35}\text{CoO}_2$: Absence of Small Hole Pockets. *J. Phys. Soc. Jpn.* **74**, 2161 (2005).
 - ³⁶ Kubo, K., Pairing symmetry in a two-orbital Hubbard model on a square lattice. *Phys. Rev. B* **75**, 224509 (2007).
 - ³⁷ Mazin, I.I., Singh, D.J., Johannes, M.D. & Du, M.H. Unconventional Superconductivity with a Sign Reversal in the Order Parameter of $\text{LaFeAsO}_{1-x}\text{F}_x$. *Phys. Rev. Lett.* **101**, 057003 (2008).
 - ³⁸ Kuroki, K. *et al.* Unconventional Pairing Originating from the Disconnected Fermi Surfaces of Superconducting $\text{LaFeAsO}_{1-x}\text{F}_x$. *Phys. Rev. Lett.* **101**, 087004 (2008).
 - ³⁹ Graser, S., Maier, T.A., Hirschfeld, P.J. & Scalapino, D.J. Near-degeneracy of several pairing channels in multiorbital models for the Fe pnictides. *New J. Phys.* **11**, 025016 (2009).

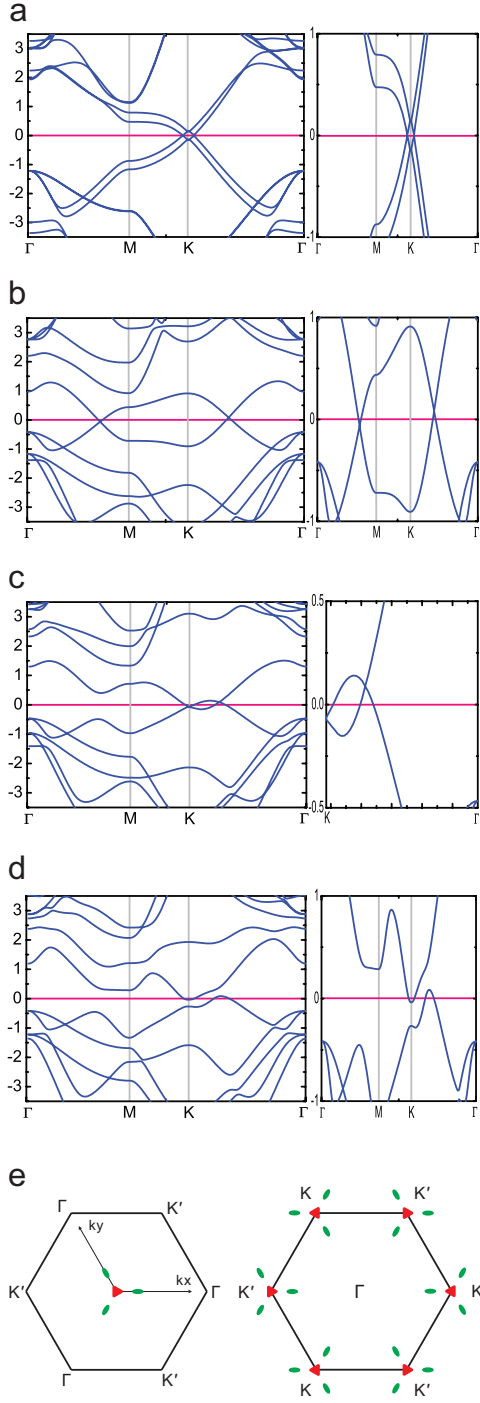


FIG. A.2. **Possible band structures for the BLS.** **a-d**, The band structures for the AA-bb (a), AA-bt (b), AB-bt (c) and AB-bb (d) respectively. Low energy zooming in for each band is also shown. **e**, Diagrams for the FS, where red(green) region stands for electron(hole).

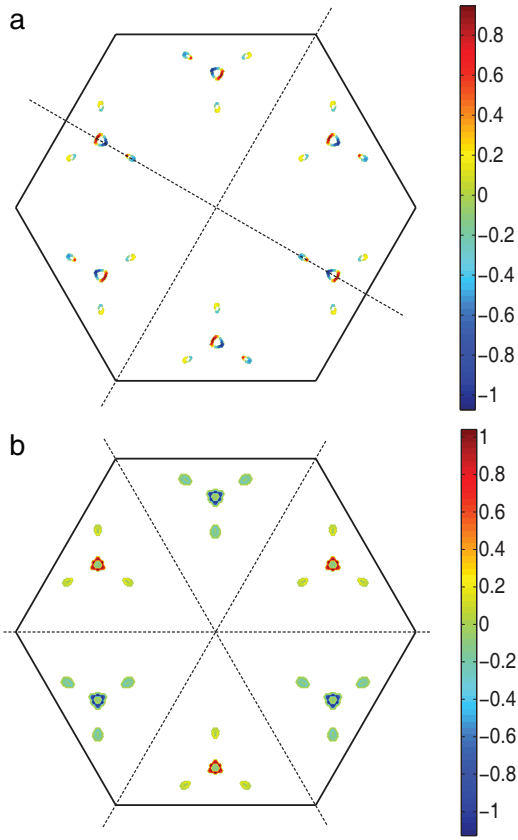


FIG. C.1. **Normalized relative gap function of the leading pairing symmetries in different channels for the undoped case.** **a**, Gap function of the d_{xy} symmetry, which is the other leading symmetry in addition to the $d_{x^2-y^2}$ pairing shown in Fig.4a of the main text. **b**, Gap function of the f-wave pairing obtained as the leading symmetry in the triplet channel.

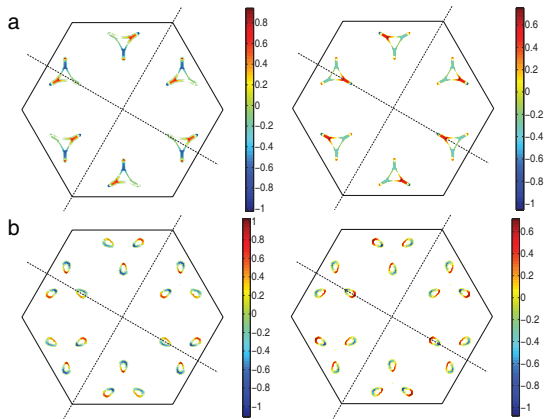


FIG. C.2. **Leading pairing symmetries for the doped cases.** **a,b**, Leading pairing symmetries of the 5% electron-doped case (a) and 5% hole-doped case (b) for $U = 1\text{eV}$. In each show, the left is the $d_{x^2-y^2}$ and the right is the d_{xy} .